

Cosmic magnetic fields with MASCLET: an application to galaxy clusters

Vicent Quilis^{1,2}, José-María Martí^{1,2} and Susana Planelles¹

¹*Departament d'Astronomia i Astrofísica, Universitat de València, E-46100 Burjassot (València), Spain*

²*Observatori Astronòmic, Universitat de València, E-46980 Paterna (València), Spain*

Released 28 February 2022

ABSTRACT

We describe and test a new version of the adaptive mesh refinement (AMR) cosmological code MASCLET. The new version of the code includes all the ingredients of its previous version plus a description of the evolution of the magnetic field under the approximation of the ideal magneto-hydrodynamics (MHD). To preserve the divergence-free condition of MHD, the original divergence cleaning algorithm of Dedner et al. (2002) is implemented. We present a set of well-known 1D and 2D tests, such as several shock-tube problems, the fast rotor and the Orszag-Tang vortex. The performance of the code in all the tests is excellent with estimated median relative errors of $\nabla \cdot \mathbf{B}$ in the 2D tests smaller than 5×10^{-5} for the fast rotor test, and 5×10^{-3} for the Orszag-Tang vortex. As an astrophysical application of the code, we present a simulation of a cosmological box of 40 comoving Mpc side length in which a primordial uniform comoving magnetic field of strength 0.1 nG is seeded. The simulation shows how the magnetic field is channelled along the filaments of gas and is concentrated and amplified within galaxy clusters. Comparison with the values expected from pure compression reveals an additional amplification of the magnetic field caused by turbulence in the central region of the cluster. Values of the order of $\sim 1 \mu\text{G}$ are obtained in clusters at $z \sim 0$ with median relative errors of $\nabla \cdot \mathbf{B}$ below 0.4%. The implications of a proper description of the dynamics of the magnetic field and their possible observational counterparts in future facilities are discussed.

Key words: magneto-hydrodynamics - methods: numerical - galaxy formation - large-scale structure of Universe - Cosmology

1 INTRODUCTION

A new era in cosmological observations favoured by forthcoming new observational facilities, such as the *Square-Kilometre Array*¹ (SKA; e.g. Keshet et al. 2004; Acosta-Pulido et al. 2015) or *ATHENA*² (e.g. Nandra et al. 2013; Barcons et al. 2017), and the already existing ones like *ALMA*³ (e.g. Wootten and Thompson 2009), will produce a huge amount of extra high-quality data, undoubtedly leading to a deeper knowledge on the processes carving the cosmic structures in the Universe.

The formation of galaxies and galaxy clusters would imprint features on the baryonic component of cosmic structures that eventually would be observable in different wavelengths of the electromagnetic spectrum. Related to these processes, shock waves, turbulence, strong gradients, and all sort of emission processes associated to the baryonic nature of the gas are expected to be observed

and quantified by the new generation of telescopes (e.g. Planelles et al. 2018).

In this context of high-quality data, the models describing the formation and evolution of such structures must also include all the relevant physical ingredients. Cosmological codes (e.g. Kravtsov et al. 1997; Teyssier 2002; Springel and Hernquist 2003; Heitmann et al. 2005; Bryan et al. 2014) have vastly improved in the last years by including all sort of processes associated to the microphysics of the gas (see Planelles et al. 2016, for a review and references therein). Although for many years it was believed that the role of \mathbf{B} was irrelevant in the formation of galaxies and galaxy clusters, nowadays, there are many observational and theoretical results pointing towards the opposite direction (see, e.g. Beck 2009; Govoni 2006; Bonafede et al. 2010; Dolag et al. 2011). In this line, the description of shock waves, strong gradients and X-ray emission, among others, would require a proper modeling of the magnetic field within current cosmological codes to compare with the observations delivered by the new generation of telescopes. This modelling should allow for the amplification of primordial weak magnetic fields via small-scale dynamo during the structure formation, and includes other astrophysical sources of magnetic seeding

¹ <https://www.skatelescope.org/>

² <http://www.the-athena-x-ray-observatory.eu>

³ <https://www.almaobservatory.org/es/inicio/>

at lower redshifts (see [Brandenburg and Subramanian \(2005\)](#) for a critical discussion on the origin of magnetic fields in clusters and a review on small-scale turbulent dynamo).

With this motivation, in recent years the most popular cosmological codes have developed updated versions incorporating the evolution of seed magnetic fields (see [Donnert et al. 2018](#), for a recent review on cosmological simulations including magnetic fields). Current cosmological smoothed particle MHD codes include those developed by [Stasyszyn et al. \(2013\)](#), the MHD extension of GADGET and [Barnes et al. \(2018\)](#), GCMHD++. [Pakmor et al. \(2011\)](#) have developed the MHD extension of AREPO ([Springel \(2010\)](#), a finite volume code using unstructured moving mesh). These codes have adapted the *divergence cleaning* (DC) algorithm of [Dedner et al. \(2002\)](#) to remove the numerical errors which otherwise would accumulate in non-soleinodal magnetic fields. Dedner’s DC method was also the algorithm implemented in the MHD version of the AMR, finite volume code ENZO ([Wang and Abel 2009](#)). An alternative to the DC algorithm is the *constrained transport* (CT) method ([Evans and Hawley 1988](#); [Balsara and Spicer 1999](#)), which satisfies the magnetic divergence constraint by construction. The CT method has been implemented in the AMR, finite-volume, MHD upgrades of RAMSES ([Fromang et al. 2006](#)), ENZO ([Collins et al. 2010](#)) and CHARM ([Miniati and Martin 2011](#)). AREPO-DG ([Guillet et al. 2019](#)) implements a discontinuous Galerkin method for ideal MHD on an Eulerian AMR grid using the *eight-wave method* of [Powell et al. \(1999\)](#), an alternative DC method to control the magnetic divergence errors.

This paper presents a new version of an already well-tested and used cosmological code, MASCLET ([Quilis 2004](#)). This new version is improved by adding the evolution of a magnetic field \mathbf{B} in the context of ideal magneto-hydrodynamics (MHD) in a full cosmological frame. Contrary to CT techniques, which evolve face-centered magnetic fields, the chosen DC method of [Dedner et al. \(2002\)](#) keeps the cell-centered discretization of the full scheme (at the cost of introducing an additional variable and the corresponding evolution equation), which makes it technically simpler to implement in the structure of the AMR code.

The paper is organized as follows. In Section 2 the basic equations to be solved are described. The implementation of the numerical techniques to solve previous equations and the details of the numerical code are presented in Section 3. In Section 4, the code is tested by carrying out a battery of numerical tests. A cosmological application is shown in Section 5, where a cosmological box including a magnetic seed is evolved. Finally, we discuss our results and offer our conclusions in Section 6.

2 EQUATIONS

2.1 The MHD equations in an expanding background

The equations of MHD ([Goedbloed and Poedts 2004](#)) describing the evolution of a magnetized fluid in a gravitational field in Eulerian coordinates (t, \mathbf{r}) are the following:

- Continuity equation:

$$\frac{\partial \rho}{\partial t} + \nabla \cdot (\rho \mathbf{u}) = 0, \quad (1)$$

- Momentum conservation:

$$\frac{\partial \rho \mathbf{u}}{\partial t} + \nabla \cdot (\rho \mathbf{u} \mathbf{u} + p^* \mathbf{I} - \mathbf{B} \mathbf{B}) = -\rho \nabla \Phi, \quad (2)$$

- Energy conservation:

$$\frac{\partial e}{\partial t} + \nabla \cdot ((e + p^*) \mathbf{u} - (\mathbf{B} \cdot \mathbf{u}) \mathbf{B}) = -\rho \mathbf{v} \cdot \nabla \Phi, \quad (3)$$

- Induction equation:

$$\frac{\partial \mathbf{B}}{\partial t} - \nabla \times (\mathbf{u} \times \mathbf{B}) = 0, \quad (4)$$

- Divergence-free condition:

$$\nabla \cdot \mathbf{B} = 0. \quad (5)$$

In these equations, ρ is the mass density, \mathbf{u} is the fluid velocity, \mathbf{B} is the magnetic field, and quantities e and p^* stand, respectively, for the total energy density (internal + kinetic + magnetic) and total pressure (thermal + magnetic):

$$e = \rho \epsilon + \frac{1}{2} \rho \mathbf{u}^2 + \mathbf{B}^2, \quad (6)$$

$$p^* = p + \frac{\mathbf{B}^2}{2}. \quad (7)$$

The thermal pressure p is related to the mass density ρ and the specific internal energy ϵ by means of an equation of state of the form $p = p(\rho, \epsilon)$. Quantity Φ appearing in the source terms of the momentum and energy equations stands for the gravitational potential.

In the presence of an expanding background, the system of Eqs. 1-5 is rewritten in terms of the comoving coordinates, $\mathbf{x} \equiv \mathbf{r}/a(t)$, where $a(t)$ is the scale factor and $H(t) \equiv \dot{a}/a$ is the Hubble constant ([Peebles 1980](#)):

$$\frac{\partial \tilde{\rho}}{\partial t} + \frac{1}{a} \nabla \cdot (\tilde{\rho} \mathbf{v}) = 0, \quad (8)$$

$$\frac{\partial \tilde{\rho} \mathbf{v}}{\partial t} + \frac{1}{a} \nabla \cdot (\tilde{\rho} \mathbf{v} \mathbf{v} + \tilde{p}^* \mathbf{I} - \tilde{\mathbf{B}} \tilde{\mathbf{B}}) = -H \tilde{\rho} \mathbf{v} - \frac{\tilde{\rho}}{a} \nabla \phi \quad (9)$$

$$\begin{aligned} \frac{\partial \tilde{E}}{\partial t} + \frac{1}{a} \nabla \cdot ((\tilde{E} + \tilde{p}^*) \mathbf{v} - (\tilde{\mathbf{B}} \cdot \mathbf{v}) \tilde{\mathbf{B}}) = \\ = -3H \tilde{p}^* + H \tilde{\mathbf{B}}^2 - H \tilde{\rho} \mathbf{v}^2 - \frac{\tilde{\rho}}{a} \mathbf{v} \cdot \nabla \phi, \end{aligned} \quad (10)$$

$$\frac{\partial \tilde{\mathbf{B}}}{\partial t} - \frac{1}{a} \nabla \times (\mathbf{v} \times \tilde{\mathbf{B}}) = -\frac{H}{2} \tilde{\mathbf{B}}, \quad (11)$$

$$\nabla \cdot \tilde{\mathbf{B}} = 0. \quad (12)$$

In this set of equations, all the spatial differential operators refer to the comoving coordinates \mathbf{x} . The overdensity with respect to the background density, ρ_B , is $\tilde{\rho} = \rho/\rho_B$. The peculiar velocity of the fluid is $\mathbf{v} = \mathbf{u} - \dot{a}\mathbf{x}$, being $\dot{a}\mathbf{x}$ the Hubble flow velocity. The quantity $\tilde{E} = E/\rho_B$ is related to the total energy density, E , of the magneto-fluid, which includes only the kinetic energy corresponding to the fluid’s peculiar velocity, i.e., $E = \rho \epsilon + \frac{1}{2} \rho \mathbf{v}^2 + \mathbf{B}^2$. The total pressure and the magnetic field are redefined as $\tilde{p}^* = p^*/\rho_B$ and $\tilde{\mathbf{B}} = \mathbf{B}/\sqrt{\rho_B}$, respectively.

The peculiar potential, $\phi = \Phi + a\mathbf{x}^2/2$, satisfies the Poisson equation

$$\Delta \phi = \frac{3}{2} H^2 a^2 \Omega \tilde{\rho} \quad (13)$$

where Ω is the density parameter.

Equations (8-10) coincide with those of [Quilis \(2004\)](#) in the case with $\tilde{\mathbf{B}} = 0$.

2.2 Divergence cleaning

MASCLET uses the divergence cleaning algorithm of [Dedner et al. \(2002\)](#) to control the magnetic field divergence errors. In the original mixed hyperbolic/parabolic correction approach of [Dedner et al. \(2002\)](#) (the one chosen in MASCLET), the divergence constraint of the magnetic field and the induction equation (in an Eulerian frame, Eqs. 4-5) are coupled by introducing an additional scalar function ψ in such a way that: i) $\nabla \cdot \mathbf{B}$ and ψ satisfy the same evolution equation, and ii) this evolution equation leads to the propagation to the domain boundaries and the decay of $\nabla \cdot \mathbf{B}$ (and ψ).

In the case of an expanding background, the original Dedner et al.'s approach can be applied once the linear $\tilde{\mathbf{B}}$ -term in Eq. 11 is removed by shifting to the comoving magnetic field $\mathbf{B}' = a^2 \sqrt{\rho_B} \tilde{\mathbf{B}}$, and the ψ -terms are introduced in Eqs. (11-12)

$$\frac{\partial \mathbf{B}'}{\partial t} - \frac{1}{a} \nabla \times (\mathbf{v} \times \mathbf{B}') + \nabla \psi = 0, \quad (14)$$

$$\frac{\partial \psi}{\partial t} + c_h^2 \nabla \cdot \mathbf{B}' = -\frac{c_h^2}{c_p^2} \psi. \quad (15)$$

Now, direct manipulation of these two equations leads to the telegraph equation for ψ (and $\nabla \cdot \mathbf{B}'$)

$$\frac{\partial^2 \psi}{\partial t^2} + \frac{c_h^2}{c_p^2} \frac{\partial \psi}{\partial t} = c_h^2 \Delta \psi \quad (16)$$

establishing that divergence errors propagate away from the point where they are produced at a speed c_h , and damp at a rate given by c_h^2/c_p^2 . Quantities c_h and c_p are dimensional parameters to be tuned (see next section for details).

Equations (14) and (15) substitute the original ones (Eqs. 11 and 12) in the system of equations. Since they are designed to ensure that $\nabla \cdot \mathbf{B}'$ (as ψ) verify the telegraph equation, the errors in $\nabla \cdot \mathbf{B}'$ propagate out of the numerical domain and damp as desired. Since $\nabla \cdot \tilde{\mathbf{B}} = \frac{1}{a^2 \sqrt{\rho_B}} \nabla \cdot \mathbf{B}' \propto (\nabla \cdot \mathbf{B}')/\sqrt{a}$, errors in $\nabla \cdot \tilde{\mathbf{B}}$ dilute in the expanding background as they propagate and damp.

3 NUMERICAL IMPLEMENTATION

3.1 The reference version of MASCLET code

MASCLET (Mesh Adaptive Scheme for Cosmological structure evolution; [Quilis 2004](#)), is a cosmological multidimensional hydrodynamic and N-body code based on an adaptive mesh refinement scheme (AMR). We address interested readers to the original paper for a complete technical description of the code and offer here a short summary of its basic ingredients.

The hydro solver is a high-order, finite volume Godunov scheme based on monotonicity preserving cell-reconstruction routines and approximate Riemann solvers. Two different cell reconstructions are implemented: a piecewise linear reconstruction with the MINMOD slope limiter, and the piecewise parabolic method PPM. Two Riemann solvers are also implemented: a Roe-type linearized Riemann solver and the HLLC Riemann solver. Advance in time is done by TVD preserving second and third order Runge-Kutta methods following a method of lines.

Dark matter is evolved using a Particle-Mesh scheme with a Lax-Wendroff temporal integrator.

Both components, gas and dark matter, evolve coupled by the

total gravitational field which is computed at each time step by solving the Poisson equation.

The gain in numerical resolution, both spatial and temporal, is obtained by means of an AMR scheme. This method refines the original coarse grid into patches whose cells are half size of their parent cells. In these new grids, all the relevant physical quantities are obtained, either by evolution of the same quantities from the previous time step, or by tri-linear interpolation from the parent grid (lower level). This process can be repeated iteratively between two consecutive levels, producing a whole hierarchy of nested grids. The criteria to decide which regions of a given grid must be refined, can be configured for every specific application (see, e.g. [Ricciardelli et al. 2013](#); [Quilis et al. 2017](#); [Planelles et al. 2018](#)).

Once the AMR hierarchy is defined, at each level, the hydro and the dark matter solvers, previously described, can be applied. The different patches at the same level and the child patches and their parents are connected through the boundary conditions and the values used to initialize them.

In the same manner, a multigrid SOR method is used to solve the Poisson equation in each patch of the hierarchy.

The current version of the code also includes inverse Compton and free-free cooling, UV heating, atomic and molecular cooling for the gas depending on the metallicity, and a phenomenological description of star formation. The description of feedback phenomena, both thermal and kinematic, from stars and active galactic nuclei is also included.

3.2 The MHD version of MASCLET code

The MHD version of MASCLET solves the system formed by Eqs. (8-10), (14) and (15) incorporating all the numerical ingredients of the reference code with the only evident modifications of the fluxes in Eqs. (8)-(10), and the addition of two new equations (Eqs. 14-15).

These equations are evolved in conservation form with numerical fluxes which, in general, depend on the eigenstructure of the system. Following the discussion in [Dedner et al. \(2002\)](#), in the one-dimensional case (the one used to obtain the eigenstructure), the system decouples into a subsystem formed by the equations for the parallel component of the magnetic field, in our case B'_\parallel , and ψ , and the usual 1D-MHD system (with a factor $1/a$ in front of the vector of fluxes) for the variables $(\tilde{\rho}, \mathbf{v}, \tilde{\mathbf{B}}_\perp, \tilde{p})$ with the magnetic field divergence-free constraint, \tilde{B}_\parallel constant.

Along the x -direction, for sufficiently large c_h , the corresponding eigenvalues of the full system, ordered in a nondecreasing sequence, are:

$$\lambda_1 = -c_h, \lambda_2 = (v^x - v_f)/a, \lambda_3 = (v^x - v_a)/a,$$

$$\lambda_4 = (v^x - v_s)/a, \lambda_5 = v^x/a, \lambda_6 = (v^x + v_s)/a,$$

$$\lambda_7 = (v^x + v_a)/a, \lambda_8 = (v^x + v_f)/a, \lambda_9 = c_h,$$

where

$$v_a = \frac{\tilde{B}^x}{\sqrt{\tilde{\rho}}} \quad (17)$$

and

$$v_{f,s} = \left\{ \frac{1}{2} \left(c_s^2 + \frac{\tilde{\mathbf{B}}^2}{\tilde{\rho}} \pm \sqrt{\left(c_s^2 + \frac{\tilde{\mathbf{B}}^2}{\tilde{\rho}} \right)^2 - 4c_s^2 v_a^2} \right) \right\}^{1/2} \quad (18)$$

are, respectively, the Alfvén speed and the fast and slow magnetosonic speeds, and c_s is the sound speed.

On the other hand, for any right eigenvector $\tilde{\mathbf{r}}_i = (\tilde{r}_i^1, \dots, \tilde{r}_i^7)^T$ of the original 1D-MHD system (Eqs. 8-10 and components y and z of Eq. 14; see e.g. [Brio and Wu 1988](#)), there is a right eigenvector of the full MHD system with the divergence correction (Eqs. 8-10, 14 and 15) $\tilde{\mathbf{R}}_i = (\tilde{r}_i^1, \dots, \tilde{r}_i^5, 0, \tilde{r}_i^6, \tilde{r}_i^7, 0)^T$ with respect to the same eigenvalue λ_i , $i = 2, 3, \dots, 8$. Moreover, two new eigenvectors appear associated to eigenvalues λ_1 and λ_9 , respectively, $\tilde{\mathbf{R}}_1 = (0, 0, 0, 0, 0, 1, 0, 0, -c_h)$ and $\tilde{\mathbf{R}}_9 = (0, 0, 0, 0, 0, 1, 0, 0, c_h)$.

In its present version, MASCLET incorporates a new slope limiter (MC, monotonic central-difference limiter; see for instance [Mignone and Bodo 2006](#)) for the piecewise linear reconstruction, and an HLL Riemann solver adapted to the MHD equations. All the results shown in this paper have been obtained with the MC slope limiter. The 1D subsystem for the variables $(\tilde{\rho}, \mathbf{v}, \tilde{\mathbf{B}}_\perp, \tilde{p})$ is evolved in time with numerical fluxes calculated with the HLL Riemann solver based on upper and lower bounds, respectively, of the largest and smallest local propagation speed of fast magnetosonic waves, λ_8, λ_2 . The decoupled subsystem for B_\parallel and ψ (in charge of the divergence cleaning) is then evolved in time with numerical fluxes based on a (constant) characteristic speed c_h chosen to be the maximum speed compatible with the time step restriction, i.e., fixed to the largest (in absolute value) propagation speed of fast magnetosonic waves, λ_2, λ_8 , across the grid. Following [Mignone and Tzeferacos \(2010\)](#), and attending to the dimensional nature of c_h and c_p , in several preliminary tests we defined $c_p = \sqrt{\Delta x c_h / \alpha}$, with $\alpha = 0.2, 0.5$ and Δx being the cell size of the finest grid. The results in the AMR applications were not satisfactory and numerical instabilities between different levels of resolution arose. The final choice was to recover Dedner's original prescription ([Dedner et al. 2002](#)) as suggested recently by [Guillet et al. \(2019\)](#) in the context on non-uniform grids, and take $c_p = \sqrt{0.18 c_h}$ (in code units). This choice of c_h and c_p is the one used in all the numerical applications presented in this paper.

4 TESTS

In this Section, we present several classical MHD tests in order to quantify the performance of the code. In all of them, there is no expanding background as in the general form of Eqs. 8-12. Consequently, these tests have been carried out by integrating the aforementioned equations with $a = 1$, $H = 0$ and $\rho_B = 1$ (in the absence of any gravitational field).

4.1 Shock-tube tests

Shock tubes have become standard tests where to prove the ability of hydrodynamical codes to describe shocks and contact discontinuities. In the case of MHD codes, the importance of shock tube tests is even greater as the solution involves a larger variety of discontinuity types (see, e.g. [Jeffrey and Taniuti 1964](#); [Takahashi et al. 2014](#)). In this section we discuss the performance of MASCLET in reproducing two representative MHD shock tube tests from [Ryu and Jones \(1995\)](#), in particular, test 2a and test 4a. In both tests, we set the adiabatic index of the equation of state to $\gamma = 5/3$, and use a one-dimensional grid with $x \in [0, 1]$. The initial discontinuity is placed at $x = 0.5$.

The tests are performed on a fixed grid with a numerical resolution of 512 zones and a piecewise linear reconstruction with the MC slope limiter. Finally, in one-dimensional tests, the divergence

free constraint is fulfilled automatically and the divergence cleaning algorithm does not operate. The numerical results are plotted as red circles whereas the analytical solutions (kindly provided by D. Ryu) appear as filled lines.

The first test is test 2a in [Ryu and Jones \(1995\)](#) with left state $\{\rho_L, v_L^x, v_L^y, v_L^z, B_L^y, B_L^z, p_L\} = \{1.08, 1.2, 0.01, 0.5, 3.6/\sqrt{4\pi}, 2/\sqrt{4\pi}, 0.95\}$ and right state $\{\rho_R, v_R^x, v_R^y, v_R^z, B_R^y, B_R^z, p_R\} = \{1, 0, 0, 0, 4/\sqrt{4\pi}, 2/\sqrt{4\pi}, 1\}$, and $B^x = 2/\sqrt{4\pi}$, involving a three-dimensional magnetic field and flow velocity. The solution at $t = 0.2$ is shown in Fig. 1. Fast shocks, rotational discontinuities (where the transverse magnetic field changes its direction) and slow shocks propagate from each side of the contact discontinuity. Despite the thinness of some structures, all the constant states and discontinuities are properly captured and only tiny numerical oscillations and overshootings are seen in some quantities in the post-shock states.

The second test is test 4a in [Ryu and Jones \(1995\)](#) with left state $\{\rho_L, v_L^x, v_L^y, v_L^z, B_L^y, B_L^z, p_L\} = \{1, 0, 0, 0, 1, 0, 1\}$ and right state $\{\rho_R, v_R^x, v_R^y, v_R^z, B_R^y, B_R^z, p_R\} = \{0.2, 0, 0, 0, 0, 0, 0.1\}$, and $B^x = 1$. The solution at $t = 0.15$ is shown in Fig. 2. This test is a *planar* Riemann problem in which the initial transverse magnetic fields and velocities are confined in a plane. In this case, the Alfvén waves, which rotate the fields, do not emerge. From left to right, the solution produces a fast and a slow rarefaction, a contact discontinuity, a slow shock and a fast, *switch-on* shock (where the transverse magnetic field turns on behind the shock). As in the previous case, the code captures the analytical solution correctly with only small overshootings at discontinuities and at the end points of the rarefaction waves.

4.2 The fast rotor

The rotor problem ([Balsara and Spicer 1999](#)) aims to test the propagation of strong torsional Alfvén waves. A dense, rapidly spinning disk rotates rigidly in a light static ambient medium. Both disk and ambient fluids are threaded by an initially uniform magnetic field. The rapid rotation of the rotor causes torsional Alfvén waves to propagate into the ambient fluid reducing the angular momentum of the rotor and hence its rotation velocity. At the same time, the magnetic field lines wrapped along the surface of the rotor increase the magnetic pressure compressing the fluid in the rotor and giving it an oblong shape.

The numerical domain for this test consists of a two-dimensional squared grid of unit length with zero-gradient boundary conditions. A rotating disk of radius r_0 is embedded in a homogeneous ambient fluid with a transition layer between r_0 and r_1 ($> r_0$). In Cartesian (x, y) coordinates, the initial conditions are given by $\{\rho, v^x, v^y\} = \{10, -\omega y, \omega x\}$ for $r = \sqrt{x^2 + y^2} \leq r_0$, and $\{\rho, v^x, v^y\} = \{1, 0, 0\}$ for $r \geq r_1$. For $r \in [r_0, r_1]$ a transition layer is set with $\{\rho, v^x, v^y\} = \{1 + 9f, -f \omega y r_0/r, f \omega x r_0/r\}$ where $\omega = 20$, $f = (r_1 - r)/(r_1 - r_0)$, and $r_0 = 0.1$, $r_1 = 0.115$. The thermal pressure is constant with $p = 1$ throughout the grid and the magnetic field is uniform and aligned with the x axis ($B^x = 5/\sqrt{4\pi}$). An ideal gas equation of state with $\gamma = 1.4$ is used. As in the previous tests, a , H and ρ_B are set to 1, 0, 1, respectively.

Figure 3 shows the density (top row) and magnetic pressure (bottom row) distributions at time $t = 0.15$ (when the torsional Alfvén waves are about to reach the grid boundaries) with two numerical resolutions: a fixed grid with 512×512 cells and an AMR grid with a coarse grid of 128×128 cells and two levels of refine-

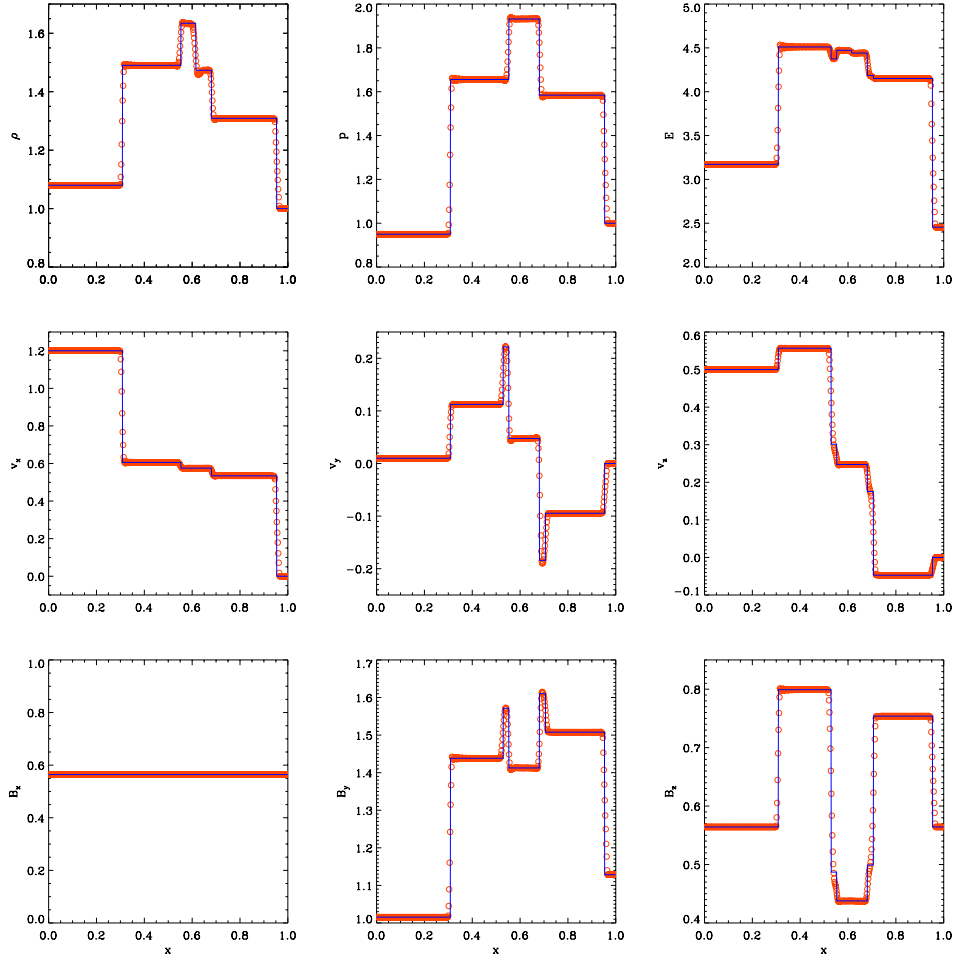


Figure 1. Test 2a of Ryu and Jones (1995) (initial data: see Section 4.1). Fast shocks, rotational discontinuities and slow shocks propagate from each side of the contact discontinuity. From top to bottom and from left to right, the panels show the mass density, gas pressure, total energy, the three components (x , y and z) of the flow velocity and the three components of the magnetic field at $t = 0.2$. Numerical results (red circles) are plotted on top of the analytical solution (blue line).

ment (refinement factor 2; effective resolution 512×512 cells). The piecewise linear reconstruction with the MC limiter is used.

Both simulations resolve the structure of the flow (high-density shell at the rotor's oblong surface just behind the high-magnetic pressure barrier; outgoing torsional Alfvén waves) with the same detail (see, e.g. Mignone and Tzeferacos 2010; Guillet et al. 2019, for comparison).

Following, for instance Collins et al. (2010) and Stasyszyn et al. (2013), we define a dimensionless quantity that could be interpreted as a relative error of the divergence of the magnetic field, $|\nabla \cdot \mathbf{B}_i| \Delta x_i / |\mathbf{B}_i|$, where \mathbf{B}_i is the magnetic field in the i cell, $\nabla \cdot \mathbf{B}_i$ is the value of the divergence computed numerically in that cell, and Δx_i is the cell width. In order to show the performance of our numerical scheme, we present Figure 4 where a map of the relative error of the $\nabla \cdot \mathbf{B}$ for our best numerical resolution run is shown at 0.15 time units. Largest errors appear associated to and move with magnetic field discontinuities.

Complementary to Fig. 4 which offers a description of the distribution and magnitude of the numerical error of the magnetic field divergence, we present a statistical analysis in Figure 5, where yellow, blue, orange and green lines indicate the upper bound errors

for 25, 50, 75 and 90% of the cells as a function of time, in the AMR run. Most of the cells (more than 90%) have divergence errors smaller than 10^{-3} along the simulation. The maximum error of the divergence (black line) remains stable at about 10%. These errors values are in fair agreement with those shown by Guillet et al. (2019) for an AMR run using divergence cleaning.

4.3 Orszag-Tang vortex

The initial state of the Orszag-Tang vortex (Orszag and Tang 1979) consists of two magnetic field loops embedded into a large-scale rotating flow structure on a two-dimensional box of unit length with periodic boundary conditions. In the subsequent evolution, complex, small-scale structures are formed. It has become a standard test to probe the accuracy of MHD codes when simulating the formation and interaction of MHD shock waves and the transition to two-dimensional MHD turbulence.

In Cartesian (x, y) coordinates, the initial conditions are $\{\rho, v^x, v^y, B^x, B^y, p\} = \{\rho_0, -v_0 \sin(2\pi y), v_0 \sin(2\pi x), -B_0 \sin(2\pi y), B_0 \sin(4\pi x), p_0\}$ with $\rho_0 = 25/(36\pi)$, $v_0 = 1$, $B_0 = 1/\sqrt{4\pi}$, $p_0 = 5/(12\pi)$,

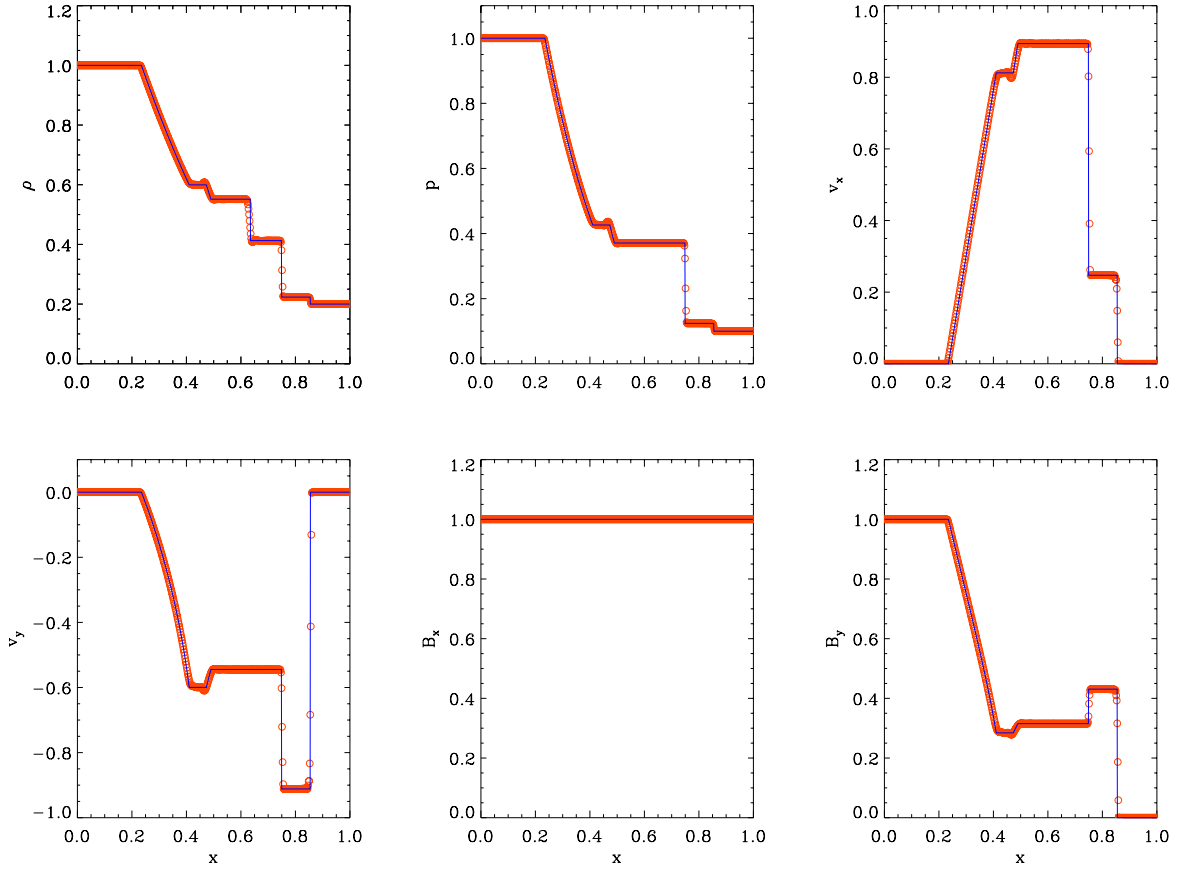


Figure 2. Test 4a of [Ryu and Jones \(1995\)](#) (planar Riemann problem; initial data: see Section 4.1). In this test, the initial transverse magnetic fields and velocities are confined in a plane. The solution produces left-propagating fast and slow rarefactions, a contact discontinuity, and right-propagating slow and fast (switch-on) shocks. From top to bottom and from left to right, the panels show the mass density, gas pressure, and x and y components of the flow velocity and the magnetic field at $t = 0.15$. Numerical results (red circles) are plotted on top of the analytical solution (blue line).

and an ideal gas equation of state with adiabatic index $\gamma = 5/3$. As in the previous tests, we set $\{a, H, \rho_B\} = \{1, 0, 1\}$ in the code equations. Figure 6 shows the density (top row) and magnetic pressure (bottom row) distributions at time $t = 0.5$ with three numerical resolutions: a fixed grid of 128×128 cells, a fixed grid with 512×512 cells and an AMR grid with a coarse grid of 128×128 cells and two additional levels of refinement with a refinement factor of 2 (for an effective resolution of 512×512 cells). The piecewise linear reconstruction with the MC limiter is used.

As it is clearly seen, the AMR run captures the small structures with the same degree of detail than the 512×512 cells fixed grid run. Additionally, the agreement between our result and previous published works is excellent (e.g. [Ryu et al. 1998](#); [Londrillo and Del Zanna 2000](#); [Fromang et al. 2006](#); [Collins et al. 2010](#); [Guillet et al. 2019](#)).

The zero-gradient boundary conditions used, as well as the fact that a non-negligible fraction of the cells are only slightly perturbed along the simulation, favour that the magnetic field divergence errors remain small in the rotor test. In the Orszag-Tang vortex test, on the contrary, all the cells are largely perturbed in the course of the evolution. This, together with the periodic boundary conditions used in this test (similar to those used in standard cosmological simulations), makes the Orszag-Tang vortex harder from

the point of view of the magnetic divergence errors⁴ but also more meaningful.

Figure 7 displays a map of the relative error of the divergence of \mathbf{B} for the best numerical resolution run. As in the fast rotor test, the largest numerical errors appear associated with flow discontinuities and do not accumulate in special locations of the domain. In order to know the time behaviour of the numerical errors, Fig. 8 shows the normalized divergence of the magnetic field for the AMR run as a function of time. As in the previous test, yellow, blue, orange and green lines indicate the upper bound error for 25, 50, 75 and 90% of the cells along the evolution. These errors, within 10^{-4} and 10^{-2} , tend to stabilize towards the end of the simulation. The black line represents the maximum error (of order 1) along time. Compared with the divergence error in the rotor test, the median error in this test is about one order of magnitude larger but still reasonably small ($\sim 0.4\%$). The maximum error compares well with the one obtained by [Guillet et al. \(2019\)](#) for the same test with an AMR run using divergence cleaning and is about a factor

⁴ Whereas the zero-gradient boundary conditions used in the rotor test let the outgoing divergence errors driven by the hyperbolic term leave the numerical grid, the periodic boundary conditions imposed in the Orszag-Tang vortex reintroduce them continuously into the computational domain (although damped).

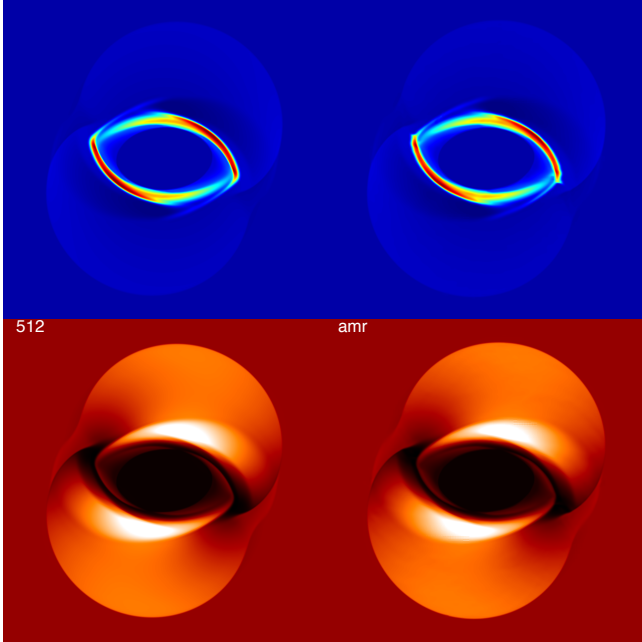


Figure 3. Rotor test. The figure shows the density (top row) and magnetic pressure – in arbitrary units – distributions (bottom row) at time $t = 0.15$ with two numerical resolutions: a fixed grid with 512×512 cells (left) and an AMR grid with a coarse grid of 128×128 cells and two levels of refinement (refinement factor 2).

of ten the one reported by Stasyszyn et al. (2013) with an SPMHD code using divergence cleaning.

5 A COSMOLOGICAL APPLICATION: MAGNETIC FIELDS IN GALAXY CLUSTERS

A straightforward application of a cosmological code would be to simulate the evolution of a cosmic volume where a large number of cosmic structures, spanning a huge range in masses and sizes, form and evolve. Thus, as an example of application of the new version of the code MASCLET, we present the results for a simulation of a computational box representing a moderate volume of the Universe.

The simulation assumes a spatially flat Λ CDM cosmology, with these cosmological parameters: $\Omega_m = 0.31$, $\Omega_\Lambda = \Lambda/3H_0^2 = 0.69$, $\Omega_b = 0.048$, $h = H_0/(100 \text{ km s}^{-1} \text{ Mpc}^{-1}) = 0.678$, $n_s = 0.96$ and $\sigma_8 = 0.82$. The simulated region is discretised with 128^3 cubical cells within a cube of comoving side length 40 Mpc. Employing a CDM transfer function from Eisenstein and Hu (1998), we set up the initial conditions at $z = 100$. We applied a constrained realization in order to generate a rich galaxy cluster in the center of the box (see Hoffman and Ribak 1991).

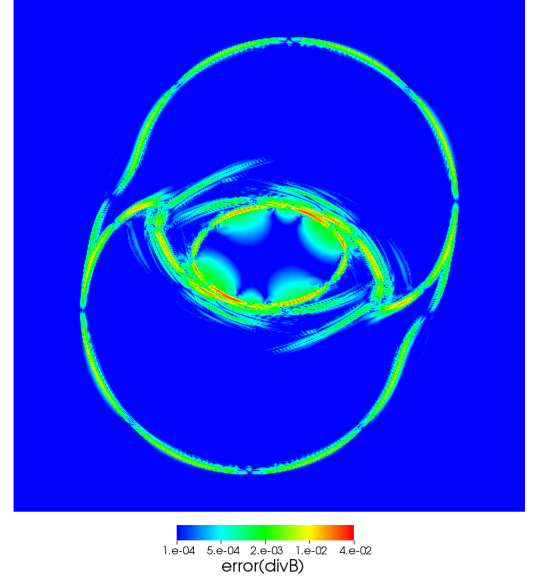


Figure 4. Map of the relative error of $\nabla \cdot \mathbf{B}$ (see text for the definition) in the rotor test at 0.15 time units for our simulations at the best resolution.

From the initial conditions, evolved until present time using a low resolution domain, we select regions satisfying some refining criteria in order to arrange three refinement levels ($l = 1, 2$, and 3) for the AMR scheme. In these initially refined levels, the dark matter (DM) component is sampled with DM particles 8, 64, and 128 times, respectively, lighter than those used to sample regions in the coarse grid ($l = 0$). As the evolution proceeds, the total density, that is baryonic plus dark matter densities, is used to refine regions on the different grids by means of a pseudo-Lagrangian approach in which a cell is flagged as refinable if its density increases in a factor of eight.

In the present simulation we use a maximum of seven refinement levels ($l = 7$), allowing for a peak physical spatial resolution of ~ 3 kpc at $z = 0$. Four different particles species are considered for the DM, corresponding to those particles on the coarse grid and those within the three first levels of refinement. The best mass resolution is $\sim 2 \times 10^6 M_\odot$, equivalent to use 1024^3 particles in the whole computational domain.

The simulation is adiabatic, therefore, no cooling or heating processes are considered. The gas is described as an ideal fluid with an adiabatic exponent equal to 5/3.

We mimic the primordial cosmological magnetic field by seeding a comoving homogenous magnetic field, \mathbf{B}_0 , filling the whole computational domain and orientated along one of the axis

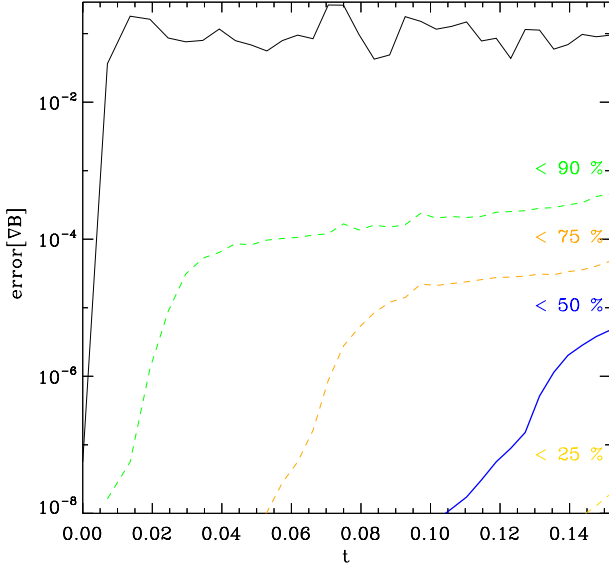


Figure 5. Relative error of $\nabla \cdot \mathbf{B}$ (see text for the definition) in the rotor test as a function of time. Yellow, blue, orange and green lines indicate the upper bound error for 25, 50, 75 and 90% of the cells. The black line represents the maximum error of the divergence.

of the computational box. The chosen value of this seed is 0.1 nG, which is just below observational constraints imposed by the analysis of CMB data (e.g. Subramanian 2016; Planck Collaboration et al. 2016). This choice of the initial magnetic field is somehow arbitrary and neglects many other possible sources of this initial field. Nevertheless, for the purpose of this paper and for the sake of comparison with previous works, we consider this value reasonable enough. Although a different choice could have an impact in the final value of \mathbf{B} if no evidences of dynamo amplification were found. Some recent works have also proved that the initial topology of the magnetic field has no relevant effects on the formation of cosmic structures such as galaxies and galaxy clusters (e.g. Marinacci et al. 2015; Vazza et al. 2017, 2018; Domínguez-Fernández et al. 2019).

In terms of the simplicity of the physics involved (only cosmic expansion, gravity and magnetohydrodynamics), the mass of the formed cluster and the effective numerical resolution, our simulation can be compared with the one with the highest numerical resolution discussed in Vazza et al. (2018). Figure 9 shows two thin slices (~ 8 kpc width) of the gas density (left panel) and the magnetic field strength (right panel) at $z \sim 0$. The slices cut the cluster centre and have a size of four virial radius approximately. The density plot exhibits a prominent core, as expected in an adiabatic simulation, corresponding to a galaxy cluster with a mass of $4 \times 10^{14} M_{\odot}$ and a virial radius $R_{\text{vir}} = 1.96$ Mpc. The comoving magnetic field intensity, B , shows a more complex structure as a consequence of the entanglement of the magnetic field lines,

specially within the virial radius. The similarity of this plot (characterized by entangled tongues of alternating high and low magnetic field) with the corresponding one in Vazza et al. (2018) (see their Figure 2) is remarkable.

In order to visualize the topology and structure of the magnetic field and its time evolution, we display the Fig. 10. The four panels present the magnetic field lines in a cubic region centred at the cluster position at $z \sim 0$ with a side length of 8 comoving Mpc ($\sim 4R_{\text{vir}}$). The lines are colour-coded according to the value of magnetic field intensity in μG . Four epochs, corresponding to redshifts $z = 2, 1, 0.5$, and 0 are displayed. It is clearly visible how, as the cluster builds up, the magnetic field is amplified in the region within the virial radius. Based on the properties of the magnetic field, the cluster can be separated into two broad regions. Within the virial radius, although the distribution of magnetic field lines is complex and intricate, the intensity of \mathbf{B} is rather homogenous with values of the order of μG . By contrast, at the cluster's outskirts, field lines basically follow the filaments of gas feeding the cluster, and the value of B in these regions is remarkably lower compared with values at the inner parts.

The radial profile of the magnetic field is presented in Fig. 11, where its mass-weighted comoving intensity is plotted against cluster-centric distance (continuous red line) in units normalized to the cluster virial radius, R_{vir} . For the sake of comparison, we also plot the magnetic field intensity that would be expected from a pure compression of the magnetic field lines (discontinuous red line). The values of B in this case can be computed as $B = B_0(\rho/\bar{\rho})^{2/3}$, where $B_0 = 0.1$ nG is the comoving magnetic field, and ρ and $\bar{\rho}$ are, respectively, the gas density and the average gas density in the whole computational box.

Our results show a B profile which is above the expected profile for magnetic fields from pure compression of the gas. The computed magnetic field is in fact 2 to 10 times higher than the one estimated from pure compression for most of the cluster volume, $r > 0.1R_{\text{vir}}$ (at the very inner centre of the cluster, $r < 0.1R_{\text{vir}}$, the profile of B presents a more complex structure with a peak and a central dip which we associate with the particular dynamical state of the simulated cluster). This magnetic field amplification is in contrast with the results for the adiabatic simulation displayed by Dubois and Teyssier (2008) (see their Figure 3). In this case, the magnetic field at the inner parts of the cluster is below the expected values from $B \propto \rho^{2/3}$. The authors attribute these results to numerical dissipation and invoke cooling processes – which resumes gravitational contraction and shearing motions – to amplify the magnetic field.

As we already advanced, our results are much more in agreement with those of Vazza et al. (2018). In this work, considering also an adiabatic simulation with a comparable effective numerical resolution, the authors manage to amplify the magnetic field to values of the order of μG (starting from a seed field of 0.1 nG) and typically one order of magnitude above the value expected if the field purely follows the gas ($B \propto \rho^{2/3}$). According to these authors, at the highest spatial resolution (≈ 4 kpc) the numerical dissipation of their code is small enough to resolve the small-scale turbulent dynamo process. In this process, the magnetic field lines are stretched following the fluid particles random motions until diffusion stops the amplification. It is then critical for the success of the process that i) numerical viscosity remains small enough to let the code maintain turbulent motions at the required spatial scales, and ii) numerical magnetic resistivity remains small enough to let the turbulent flow stretch the magnetic field lines efficiently before non-ideal effects kill the process. The similarity of the magnetic

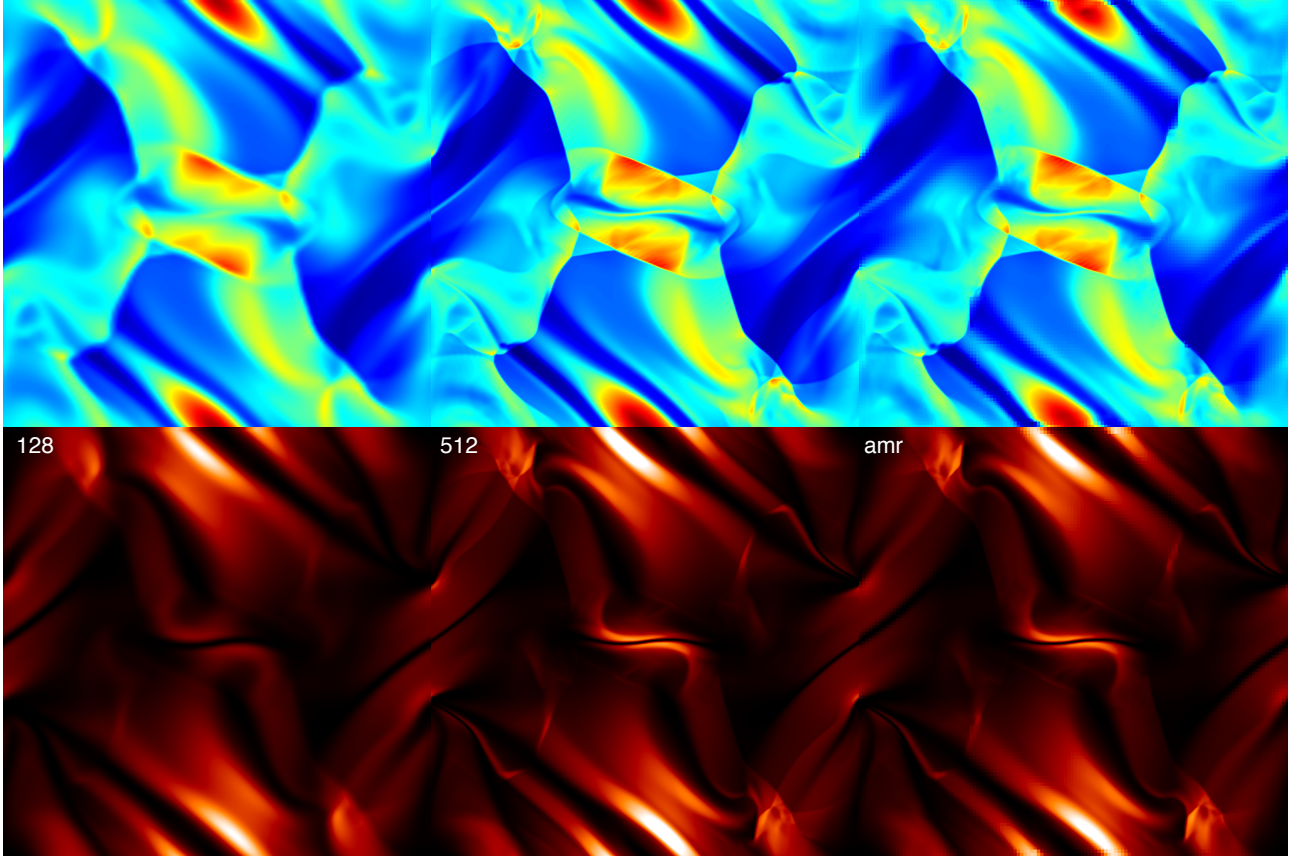


Figure 6. Orszag-Tang test. The figure shows the density (top row) and magnetic pressure (bottom row) – in arbitrary units – distributions at time $t = 0.5$ with three numerical resolutions. From left to right: a fixed grid of 128×128 cells, a fixed grid with 512×512 cells and an AMR grid with a base grid of 128×128 cells and two additional levels of refinement with a refinement factor of 2.

intensity distribution shown in Fig. 9 with the corresponding one in Vazza et al. (2018) (Fig. 2), might point to the same process as the responsible of the additional magnetic field amplification seen in Fig. 9. This should be verified in future works. As a first step, we have confirmed that the modulus of the vorticity (not shown) and the magnetic field intensity are closely correlated, pointing to turbulence as the origin of the added field amplification.

To assess the performance of our code in keeping magnetic field divergence errors under control, and as in previous sections, we study the normalized divergence of the comoving magnetic field, \mathbf{B} . In this particular test, we modify the definition of this quantity to reduce the weight of spurious values associated to cells where the magnetic field intensity is very low. Following Tricco and Price (2012), we change $|\mathbf{B}_i|$ in the denominator of the normalized divergence by $|\mathbf{B}_i| + 0.01|\mathbf{B}_{\max}|$, where $|\mathbf{B}_{\max}|$ is the maximum of $|\mathbf{B}_i|$ across the numerical grid.

Figure 11 displays the median of the relative error (blue thick line), and the relative error of the 25% (yellow line), 75% (orange line), and 90% (green line) percentiles, respectively. The black line shows the maximum relative error of $\nabla \cdot \mathbf{B}$ according to the previous definition. Finally, let us note that with 90% of the numerical cells with a divergence relative error well below 3×10^{-2} in $\nabla \cdot \mathbf{B}$, the spurious magnetic energy change related to the divergence error must be of the order of $\sim 10^{-3}$ or less, i.e., much smaller than the

increase of magnetic energy associated to the added magnetic field amplification.

The most relevant structure formed in this computational box is the galaxy cluster located at the box centre. The radial profile of the average value of the error of the divergence of \mathbf{B} as a function of the cluster-centric distance is displayed as the blue line in Fig. 12. The average values are computed as volume weighted means in spherical shells. This average radial error can be compared with the average radial value of $|\mathbf{B}|$ from the simulation together with the expected value of the magnetic field intensity from a pure compression (red lines in Fig. 12). The relative error exhibits an acceptable behaviour with values below 4%.

To spot possible large errors that could be concealed in the radial average values of the normalized divergence, we present in Figure 13 a map of the error of the divergence of B in the same thin slice through the cluster centre displayed in Fig. 9. As seen in the figure, the point values of the normalized divergence in the central region of the cluster are smaller than 20% with a mean value 0.5%, in agreement with the median error shown in Fig. 11.

6 CONCLUSIONS

The role of magnetic field in cosmological scenarios has traditionally been a matter of debate. Most of the times, they have been pushed into the background as minor actors in the formation and

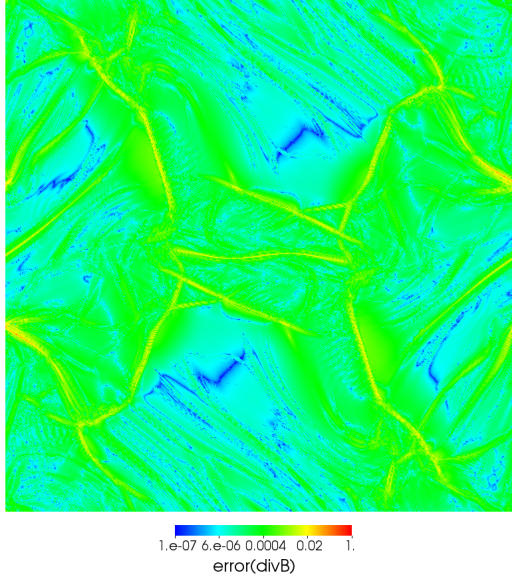


Figure 7. Map of the relative error of $\nabla \cdot \mathbf{B}$ (see text for the definition) in the Orszag-Tang test at 0.5 time units for our simulations at the best resolution.

evolution of cosmic structures, whose part was completely subdominant. However, this picture is rapidly changing in recent years. In the epoch of the so called precision cosmology, where theory and data are widening our knowledge on the formation of galaxy and galaxy clusters, the magnetic fields can play a relevant role, both in the theoretical and observational planes.

In this line, we presented a new version of an already well-tested and used cosmological code, that includes a proper description of the MHD processes. Several commonly used tests, whose solutions are perfectly known, are shown. In all of them, the performance of our code is more than satisfactory.

As a final application with cosmological interest, we followed the evolution of gas and dark matter components in a cosmic volume, where a uniform magnetic field was introduced at a very early stage of the evolution ($z \sim 100$). In this simulation, the magnetic field was amplified from its initial uniform value of $B_0 \sim 0.1$ nG until values of the order of $B \sim 1$ μ G in the most massive galaxy clusters. Our simulation shows how the magnetic field is channeled along the filament of gas and it is amplified at the structures formed at the intersections of such filaments. The topology of the magnetic field lines clearly reveals how the field lines tangle up in the galaxy clusters. The comparison between the values of B obtained in the simulation and those expected from pure compression ($B \propto \rho^{2/3}$) reveals that there is an additional process operating at the core of

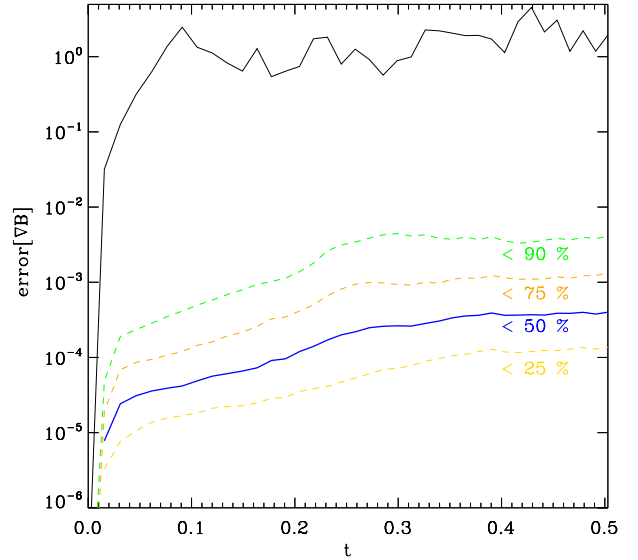


Figure 8. Relative error of $\nabla \cdot \mathbf{B}$ (see text for the definition) in the Orszag-Tang test as a function of time. Yellow, blue, orange and green lines indicate the upper bound error for 25, 50, 75 and 90% of the cells. The black line represents the maximum error of the divergence.

the cluster responsible for the extra amplification of the magnetic field. To elucidate the nature of this process, essential to understand the origin of magnetic fields in clusters of galaxies, will be the subject of future research.

It is nowadays clear that cosmic magnetic fields, although dynamically negligible, play a crucial role in shaping the physical properties of the intergalactic medium. From an observational point of view, current radio observations, such as those with JVLA or LOFAR, provide a unique tool to reveal the current distribution of magnetic fields (e.g. [Donnert et al. 2018](#), and references therein). In this sense, current and next generation of radio facilities, like the SKA and its precursors, will achieve, mainly by means of the Faraday tomography technique, an unprecedented detail in the description of the evolution and distribution of cosmic magnetic fields. From a theoretical point of view, while in the last years cosmological simulations have been significantly improved in terms of the development of different feedback models to explain galaxy formation, a proper numerical understanding of cosmic magnetic fields and gas turbulence phenomena remains as a challenge. Therefore, in order to interpret future radio observations and to shorten the existing distance between the observational and the theoretical planes, an accurate and ‘realistic’ description of cosmic magnetic fields in full cosmological simulations seems to be imperative.

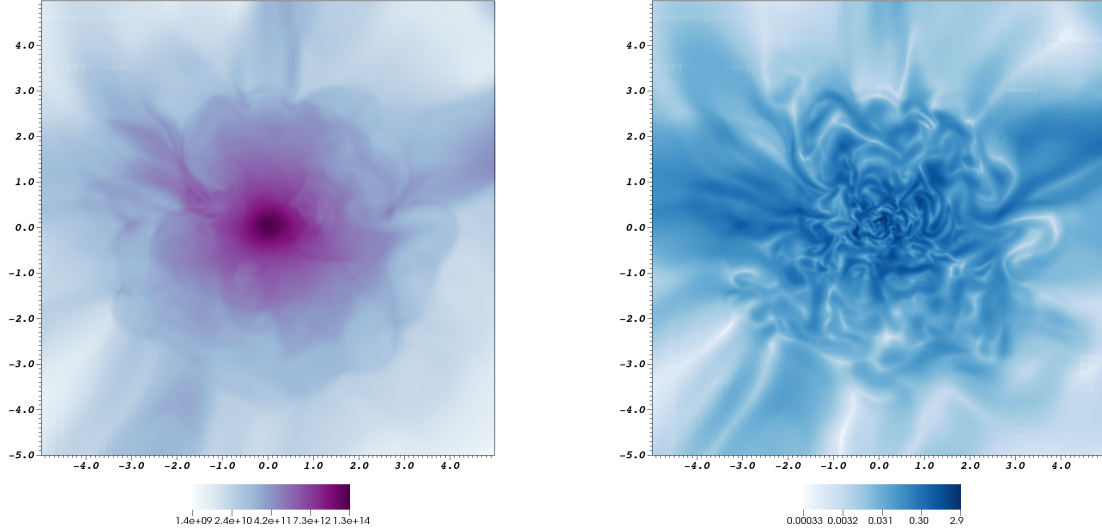


Figure 9. Slices (~ 8 kpc width) through the cluster center for density (left) and B (right) at $z \sim 0$. The density is in units of M_{\odot}/Mpc^3 and the comoving magnetic field intensity, B , is in μG . The spatial scales are in comoving Mpc.

ACKNOWLEDGEMENTS

This work has been supported by the Spanish Ministerio de Ciencia, Innovación y Universidades (MICINN, grant AYA2016-77237-C3-3-P) and by the Generalitat Valenciana (grant PROMETEO/2019/071). JMM also acknowledges partial support from MICINN (grant PGC2018-095984-B-I00). The authors are indebted to D. Ryu and T.W. Jones for providing them with the analytical solutions for the one-dimensional tests shown in the paper and acknowledge fruitful discussions with P. Cerdá-Durán. We thank the anonymous referee for his/her constructive criticism. Simulations have been carried out using the supercomputer Lluís Vives at the Servei d'Informàtica of the Universitat de València.

REFERENCES

- Acosta-Pulido J.A., et al., 2015, ArXiv e-prints
 Balsara D.S., Spicer D.S., 1999, *Journal of Computational Physics*, 149, 270
 Barcons X., et al., 2017, *Astronomische Nachrichten*, 338, 153
 Barnes D.J., On A.Y.L., Wu K., Kawata D., 2018, *MNRAS*, 476, 2890
 Beck R., 2009, *Astrophysics and Space Sciences Transactions*, 5, 43
 Bonafede A., Feretti L., Murgia M., Govoni F., Giovannini G., Dallacasa D., Dolag K., Taylor G.B., 2010, *A&A*, 513, A30
 Brandenburg A., Subramanian K., 2005, *Phys. Rep.*, 417, 1
 Brio M., Wu C.C., 1988, *Journal of Computational Physics*, 75, 400
 Bryan G.L., et al., 2014, *The Astrophysical Journal Supplement Series*, 211, 19
 Collins D.C., Xu H., Norman M.L., Li H., Li S., 2010, *ApJS*, 186, 308
 Dedner A., Kemm F., Kröner D., Munz C.D., Schnitzer T., Wessberg M., 2002, *Journal of Computational Physics*, 175, 645
 Dolag K., Kachelriess M., Ostapchenko S., Tomàs R., 2011, *ApJ*, 727, L4
 Domínguez-Fernández P., Vazza F., Brüggén M., Brunetti G., 2019, *MNRAS*, 486, 623
 Donnert J., Vazza F., Brüggén M., ZuHone J., 2018, *Space Sci. Rev.*, 214, 122
 Dubois Y., Teyssier R., 2008, *A&A*, 482, L13
 Eisenstein D.J., Hu W., 1998, *ApJ*, 496, 605
 Evans C.R., Hawley J.F., 1988, *ApJ*, 332, 659
 Fromang S., Hennebelle P., Teyssier R., 2006, *A&A*, 457, 371
 Goedbloed J.P.H., Poedts S., 2004, *Principles of Magnetohydrodynamics*
 Govoni F., 2006, *Astronomische Nachrichten*, 327, 539
 Guillet T., Pakmor R., Springel V., Chandrasekar P., Klingenberg C., 2019, *MNRAS*, 485, 4209
 Heitmann K., Ricker P.M., Warren M.S., Habib S., 2005, *The Astrophysical Journal Supplement Series*, 160, 28
 Hoffman Y., Ribak E., 1991, *ApJ*, 380, L5
 Jeffrey A., Taniuti T., 1964, *Non-linear wave propagation*
 Keshet U., Waxman E., Loeb A., 2004, *ApJ*, 617, 281
 Kravtsov A.V., Klypin A.A., Khokhlov A.M., 1997, *The Astrophysical Journal Supplement Series*, 111, 73
 Londrillo P., Del Zanna L., 2000, *ApJ*, 530, 508
 Marinacci F., Vogelsberger M., Mocz P., Pakmor R., 2015, *MNRAS*, 453, 3999
 Mignone A., Bodo G., 2006, *MNRAS*, 368, 1040
 Mignone A., Tzeferacos P., 2010, *Journal of Computational Physics*, 229, 2117
 Miniati F., Martin D.F., 2011, *ApJS*, 195, 5
 Nandra K., et al., 2013, ArXiv e-prints
 Orszag S.A., Tang C.M., 1979, *Journal of Fluid Mechanics*, 90, 129

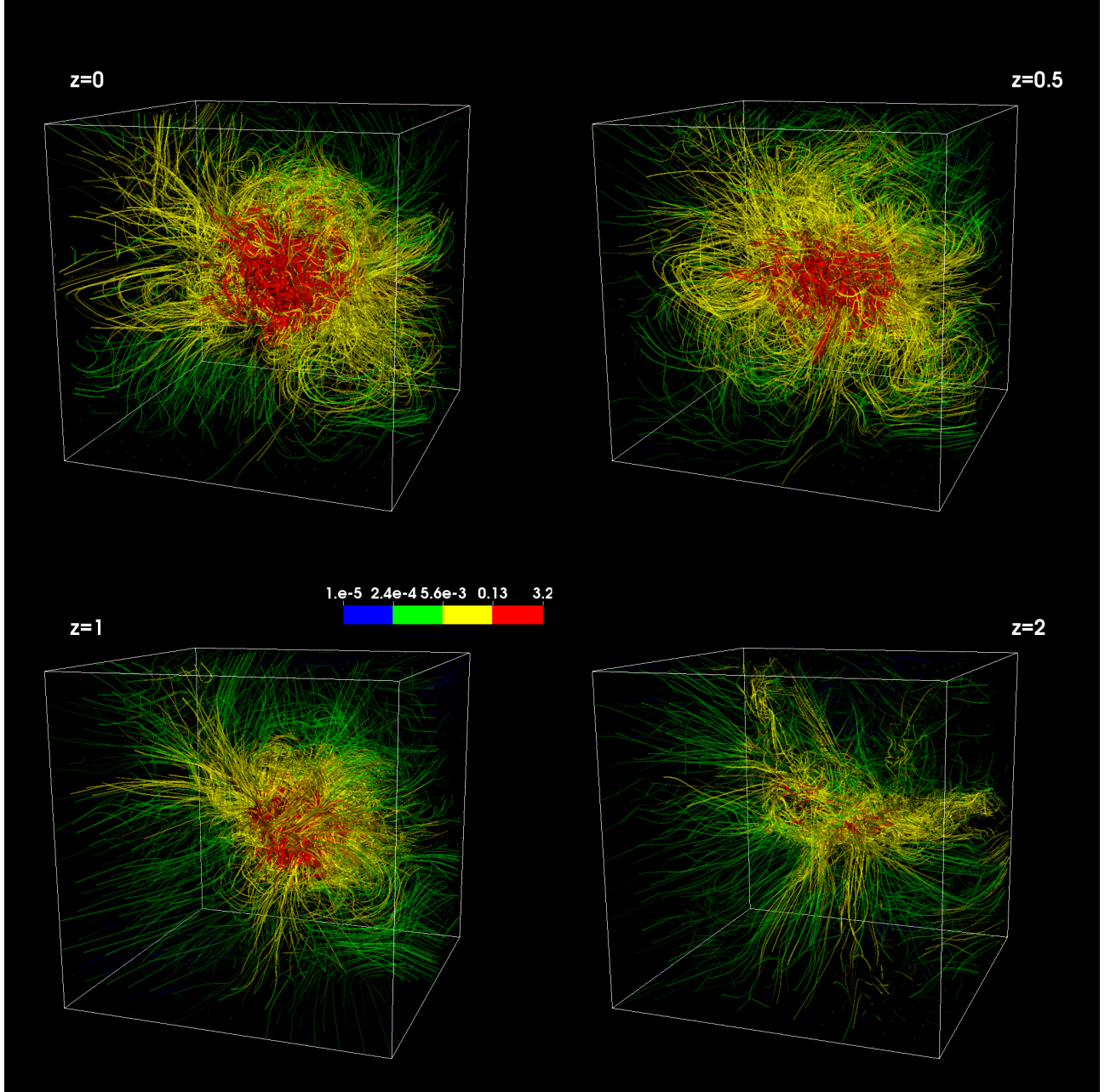


Figure 10. Magnetic field lines distribution at four redshifts, 2, 1, 0.5, and 0 in a box centred at the cluster with a side length of eight comoving Mpc (four virial radius). The lines are colour-coded according with the value of the comoving magnetic field in units of μG . MNRAS **000**, 1–13 (2019)

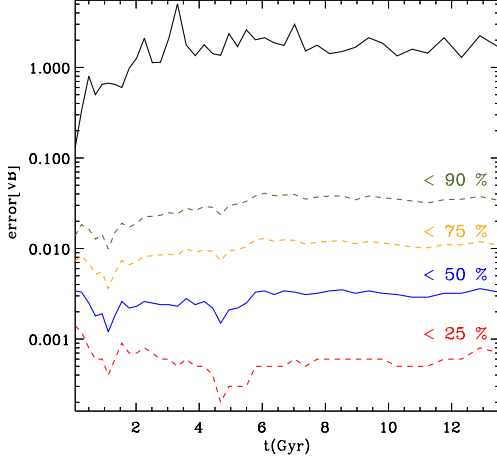


Figure 11. Relative error of the divergence of the comoving magnetic field as a function of cosmic time. Yellow, blue, orange and green lines indicate the upper bound error for 25, 50, 75 and 90% of the cells. The black line represents the maximum error of the divergence.

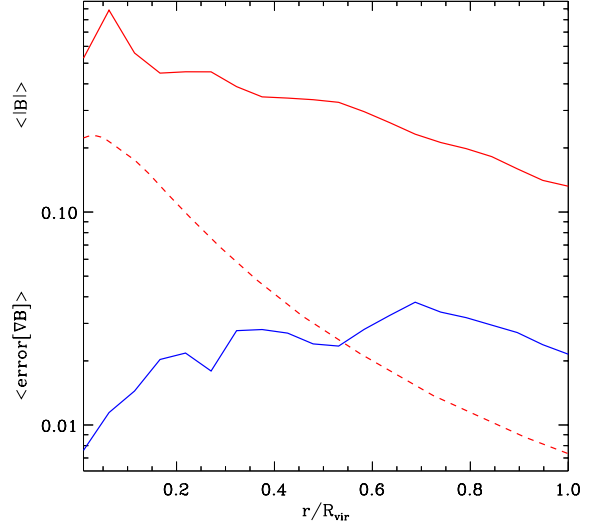


Figure 12. Radial profile of the comoving magnetic field intensity (in μG) as a function of the cluster-centric distance in units of virial radius (red lines). The continuous line corresponds to the profile obtained from the simulation and the red dashed line represents the value of B expected from an amplification of the magnetic field from a pure compression defined as $B = B_0(\rho/\bar{\rho})^{2/3}$. The solid blue line represents the radial profile of the average relative error of the divergence of \mathbf{B} in the same radial units

- Pakmor R., Bauer A., Springel V., 2011, MNRAS, 418, 1392
Peebles P.J.E., 1980, *The large-scale structure of the universe*
Planck Collaboration, et al., 2016, A&A, 594, A19
Planelles S., Schleicher D.R.G., Bykov A.M., 2016, *Large-Scale Structure Formation: From the First Non-linear Objects to Massive Galaxy Clusters*, pp. 93–139
Planelles S., Mimica P., Quilis V., Cuesta-Martínez C., 2018, MNRAS, 476, 4629
Powell K.G., Roe P.L., Linde T.J., Gombosi T.I., Zeeuw D.L.D., 1999, Journal of Computational Physics, 154, 284
Quilis V., 2004, MNRAS, 352, 1426
Quilis V., Planelles S., Ricciardelli E., 2017, MNRAS, 469, 80
Ricciardelli E., Quilis V., Planelles S., 2013, MNRAS, 434, 1192
Ryu D., Jones T.W., 1995, ApJ, 442, 228
Ryu D., Miniati F., Jones T.W., Frank A., 1998, ApJ, 509, 244
Springel V., 2010, MNRAS, 401, 791
Springel V., Hernquist L., 2003, MNRAS, 339, 289
Stasyszyn F.A., Dolag K., Beck A.M., 2013, MNRAS, 428, 13
Subramanian K., 2016, Reports on Progress in Physics, 79, 076901
Takahashi K., Yamada S., Yamada, 2014, Journal of Plasma Physics, 80, 255
Teyssier R., 2002, A&A, 385, 337
Tricco T.S., Price D.J., 2012, Journal of Computational Physics, 231, 7214
Vazza F., Brüggen M., Gheller C., Hackstein S., Wittor D., Hinz P.M., 2017, Classical and Quantum Gravity, 34, 234001
Vazza F., Brunetti G., Brüggen M., Bonafede A., 2018, MNRAS, 474, 1672
Wang P., Abel T., 2009, ApJ, 696, 96
Wootten A., Thompson A.R., 2009, IEEE Proceedings, 97, 1463

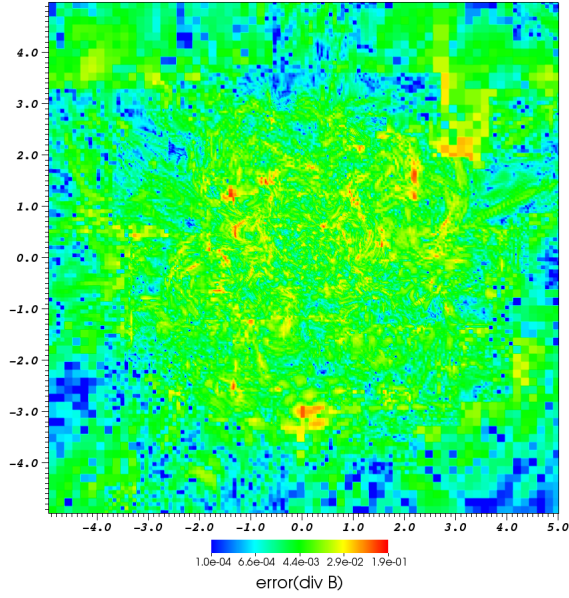


Figure 13. Slice (~ 8 kpc width) through the cluster center for the relative error of the divergence of \mathbf{B} .